Monsoon intraseasonal oscillations as simulated by the superparameterized Community Atmosphere Model

Bidyut B. Goswami,[1] Neena Joseph Mani,[1] P. Mukhopadhyay,[1] Duane E. Waliser,[2] James J. Benedict,[3] Eric D. Maloney,[3] Marat Khairoutdinov,[4] and B. N. Goswami[1]

[1]   The relative success of the Community Atmosphere Model with superparameterized convection (SP-CAM) in simulating the space-time characteristics of the Madden Julian Oscillation encourages us to examine its simulation of the Indian summer monsoon and monsoon intraseasonal oscillations (MISOs). While the model simulates the onset and withdrawal of the Indian monsoon realistically, it has a significant wet bias in boreal summer precipitation over the Asian monsoon region. The space-time characteristics of the MISOs simulated by the SP-CAM are examined in detail and compared with those of the observed MISO to gain insight into the model's bias in simulating the seasonal mean. During northern summer, the model simulates a 20 day mode and a 60 day mode in place of the observed 15 and 45 day modes, respectively. The simulated 20 day mode appears to have no observed analog with a baroclinic vertical structure and strong northward propagation over Indian longitudes. The simulated 60 day mode seems to be a lower-frequency version of the observed 45 day mode with relatively slower northward propagation. The model's underestimation of light rain events and overestimation of heavy rain events are shown to be responsible for the wet bias of the model. More frequent occurrence of heavy rain events in the model is, in turn, related to the vertical structure of the higher-frequency modes. Northward propagation of the simulated 20 day mode is associated with a strong cyclonic vorticity at low levels north of the heating maximum associated with a smaller meridional scale of the simulated mode. The simulated vertical structure of heating indicates a strong maximum in the upper troposphere between 200 and 300 hPa. Such a heating profile seems to generate a higher-order baroclinic mode response with smaller meridional structure, stronger low-level cyclonic vorticity, enhanced low-level moisture convergence, and higher precipitation. Therefore, the vertical structure of heating simulated by the cloud-resolving model within SP-CAM may hold the key for improving the precipitation bias in the model.

Citation: Goswami, B. B., N. J. Mani, P. Mukhopadhyay, D. E. Waliser, J. J. Benedict, E. D. Maloney, M. Khairoutdinov, and B. N. Goswami (2011), Monsoon intraseasonal oscillations as simulated by the superparameterized Community Atmosphere Model, *J. Geophys. Res.*, *116*, D22104, doi:10.1029/2011JD015948.

1. Introduction

[2]   Through determining the interannual variability of the seasonal mean, on one hand, and clustering of synoptic disturbances, on the other, northward propagating [e.g., *Yasunari*, 1979; *Sikka and Gadgil*, 1980] monsoon intra-seasonal oscillations (MISOs) represent major building blocks of the Indian summer monsoon (ISM) [*Goswami et al.*, 2006]. The MISO represents a signal with amplitude as large as the annual cycle and much larger than the interannual variability of the seasonal mean [*Waliser*, 2006; *Goswami et al.*, 2011]. The MISO manifests in the form of active and break spells and imparts a significant challenge and point of promise for water resource management. Hence, extended range prediction of the active and break spells has tremendous socioeconomic implications. In order for forecast models to have skill in predicting the active and break spells, they must simulate the space-time spectra of the MISO with fidelity. A space-time spectral analysis of the Indian MISO indicates an eastward propagating component with periodicity between 20 and 70 days and zonal wave

---

[1]Indian Institute of Tropical Meteorology, Pune, India.
[2]Jet Propulsion Laboratory, California Institute of Technology, Pasadena, California, USA.
[3]Department of Atmospheric Science, Colorado State University, Fort Collins, Colorado, USA.
[4]School of Marine and Atmospheric Sciences, Stony Brook University, New York, New York, USA.

numbers between 1 and 3, which is about 1.5 times stronger than the corresponding westward propagating component [see *Lin et al.*, 2008, Figure 10]. The MISO over the Indian region is also characterized by strong northward propagation that is about 4 times stronger than the corresponding southward propagating component [see *Lin et al.*, 2008, Figure 15a]. However, most climate models exhibit difficulty in simulating the MISO [*Waliser et al.*, 2003; *Lin et al.*, 2008] and underestimate the northward propagating component, in particular [see *Lin et al.*, 2008, Figure 15a]. Because of their contribution to the seasonal mean, improved MISO simulation in a model would have a beneficial impact not only on the extended range prediction of the active and break spells, but also in seasonal prediction.

[3] As the problem of better simulation of the MISOs in climate models is similar to the difficulties faced in simulating the Madden Julian Oscillation (MJO), we may gain insight from the experience of the community in attempting to improve MJO simulations. Considerable effort has been expended during the last few years to improve the poor simulation of the MJO by models [e.g., *Slingo et al.*, 2005; *Lin et al.*, 2006; *Waliser et al.*, 2009; *Kim et al.*, 2009]. In addition to efforts to improve the MJO through modifications to conventional convection parameterizations, methods involving explicit representation of some aspects of clouds have emerged to improve the poor simulation of the MJO. For example, global cloud-resolving model simulations have been conducted that produce realistic mesoscale cloud clusters and have demonstrated better simulation of the MJO [*Miura et al.*, 2007; *Sperber et al.*, 2008; *Oouchi et al.*, 2009; *Liu et al.*, 2009; *Sato et al.*, 2009]. However, due to the large computation cost of such models, the ability to simulate multiple years to analyze systematic biases in the MJO life cycle remains computationally prohibitive [*Khairoutdinov et al.*, 2008, hereafter KDR08]. Another rather attractive alternative to global-cloud resolving models is the multi-scale modeling framework (MMF) [*Khairoutdinov and Randall*, 2001; *Khairoutdinov et al.*, 2005; *Tao et al.*, 2009] that has demonstrated good simulation of MJO space-time characteristics [*Benedict and Randall*, 2009].

[4] In the MMF approach, a 2-D cloud-resolving model (CRM) is embedded with each grid column of a general circulation model (GCM) such that explicit simulation of sub-grid scale cloud processes replaces the traditional cumulus parameterization of the GCM, hence minimizing the need for imperfect parameterization assumptions. Because the CRM time step is much shorter than that of the GCM, the CRM is integrated several times in one GCM time step (for details, see *Benedict and Randall* [2009]). The horizontal average of the CRM output within a GCM grid box determines the physical tendencies for the next GCM time step.

[5] While the MMF approach has been extensively tested for simulating the eastward propagating convection anomalies from the Indian ocean to the western Pacific during boreal winter [*Benedict and Randall*, 2009], relatively little work has been conducted to address the fidelity of the MMF in simulating the northward propagating ISM intraseasonal oscillation [*Stan et al.*, 2010; *DeMott et al.*, 2011]. As the MISO and ISM forecasting remain a challenge for both statistical and dynamical approaches, and as it has significant societal impacts, the objective of this paper is to investigate the quality of the MISO simulation as obtained from an atmospheric model intercomparison project (AMIP) run of the SP-CAM. Such an analysis and comparison with the observed MISO may suggest the utility of the SP-CAM to be used as a tool for extended range prediction of the MISO or as a "laboratory" to better understand shortcomings in convection-parameterized models. In addition, as the MISO contributes significantly to the seasonal mean precipitation and winds, a diagnosis of the biases in the MISO simulation may also provide clues toward improvement of the simulation of the seasonal mean climate.

[6] The model and data used to diagnose the model are described in section 2, and simulation of the monsoon climatology is described in section 3. Basic characteristics of the monsoon intraseasonal variability (ISV) as produced by the model are presented in section 4, and a more detailed diagnosis of the simulated variability is made in section 5. This is followed in section 6 by a discussion of how biases in simulating the MISO affect the seasonal mean bias. Major conclusions are summarized in section 7.

2. Model Simulations and Data Used

[7] The National Center for Atmospheric Research (NCAR) Community Atmosphere Model version 3 (CAM 3.0) [*Collins et al.*, 2006] acts as the host GCM for the super-parameterization approach employed [e.g., *Khairoutdinov et al.*, 2005]. The version of CAM3.0 used has a 2.8° × 2.8° horizontal grid (T42 spatial truncation), 30 vertical levels up to 3.6 hPa, and a time step of 30 min. Embedded within each GCM grid cell is a 2-D CRM composed of 32 columns oriented in the north-south direction having 4 km horizontal grid spacing, periodic boundary conditions, 28 vertical levels collocated with the 28 lowest CAM levels, and a time step of 20 s. This embedded CRM effectively replaces the CAM's conventional parameterizations of moist physics, convection, turbulence, and boundary layer processes. However, coupling between the surface and atmosphere is computed only on the GCM grid. The effects of subgrid scale temperature and wind perturbations (e.g., gust fronts) on surface fluxes are thus not included. CRM scale enhancements of surface drag related to localized gustiness of near-surface winds are explicitly included, however. The AMIP simulation was conducted using prescribed monthly mean (interpolated to daily mean) sea surface temperatures and sea ice concentrations [*Hurrell et al.*, 2008]. The simulation produced 19 years of global daily output spanning 1 September 1985 to 25 September 2004.

[8] Further implementation details on the super-parameterization approach can be found in the studies by *Benedict and Randall* [2009], *Khairoutdinov* and *Randall* [2003], and *Khairoutdinov et al.* [2005]. Additional details of the SP-CAM AMIP simulation used in this study can be found in KDR08.

[9] To evaluate the simulated precipitation, the Global Precipitation Climatology Project (GPCP) rainfall data [*Huffman et al.*, 2001] regridded to the model resolution (2.8° × 2.8°) are used. The regridding is done using a bilinear interpolation technique. The GPCP data used for model validation are from 1997 to 2008. The NOAA Outgoing Longwave Radiation (OLR) data set is used to provide additional diagnostics of convective variability. Horizontal winds are taken from National Centers for Environmental
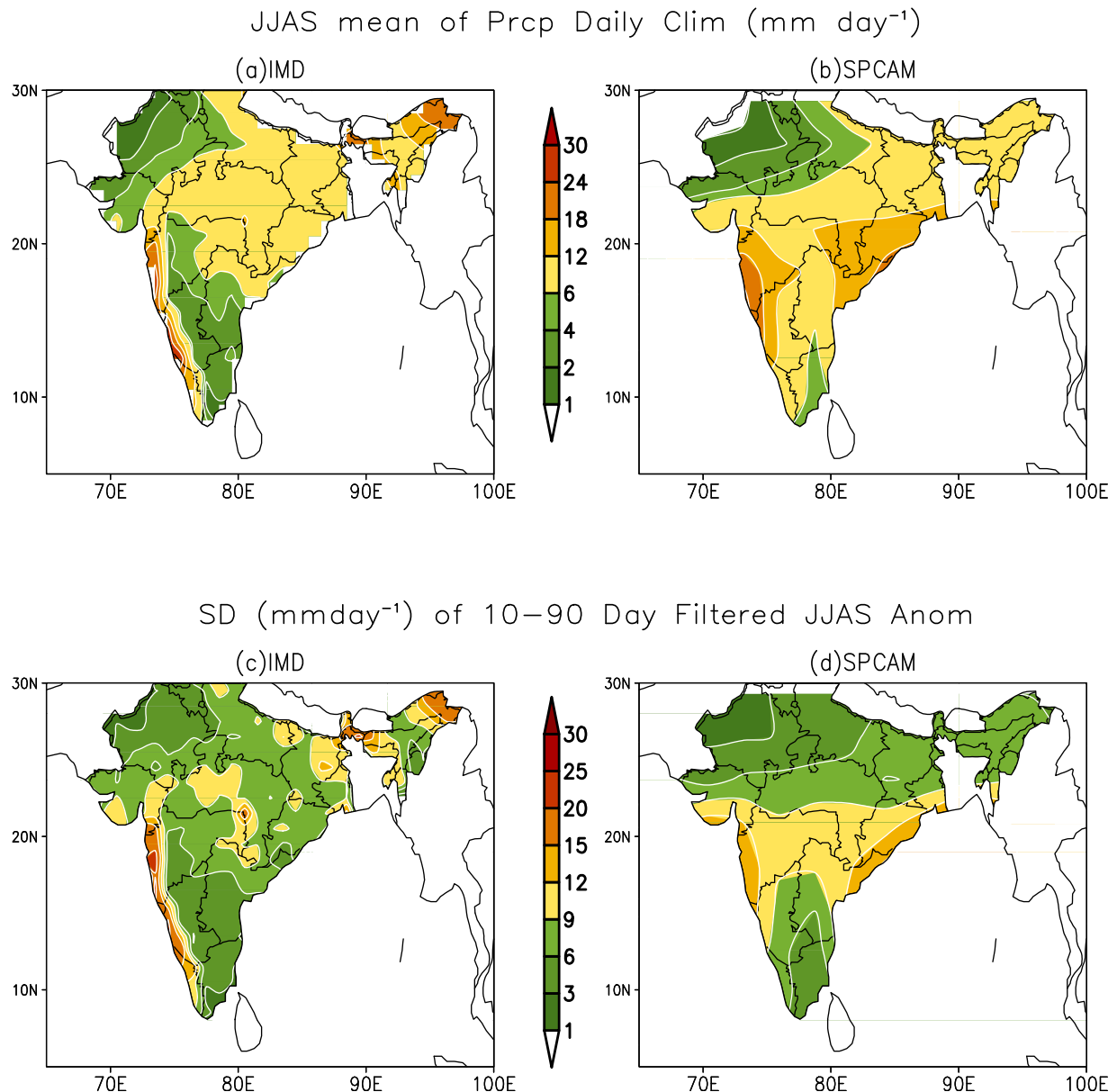
JJAS mean of Prcp Daily Clim (mm day⁻¹)

SD (mmday⁻¹) of 10−90 Day Filtered JJAS Anom

Figure 1. Climatological mean (JJAS) precipitation (mm d^{-1}) from (a) IMD and (b) SP-CAM. Standard deviation of 10–90 day bandpass-filtered daily precipitation anomalies (mm d^{-1}) (JJAS) from (c) IMD and (d) SP-CAM.

Prediction (NCEP)/NCAR reanalysis at 2.5° × 2.5° resolution [*Kalnay et al.*, 1996]. The NCEP winds and NOAA OLR data are used for 1986 to 2004.

[10] In order to extract MISOs from the simulation and observations, daily anomalies are calculated as the departure of daily values from a smoothed climatology at daily resolution. The smoothed climatology is reconstructed based on the annual mean and first three harmonics of the long-term mean seasonal cycle.

3. Simulation of Monsoon Climatology

[11] As MISOs are hypothesized to arise from a convective-radiative-dynamical feedback process [e.g., *Goswami and Shukla*, 1984; *Wang*, 2005], they critically depend on the background climatic state. Therefore, examination of the simulated climatological mean field is necessary for understanding any biases in the model MISO simulation. In this section, we present an overview of simulated climatological mean June–July–August–September (JJAS) precipitation and winds and compare them with observations.

[12] As reliable high-resolution rainfall data are available over continental India compiled by the India Meteorological Department (IMD), [*Rajeevan et al.*, 2006], we compare the climatological mean JJAS precipitation simulated by SP-CAM with IMD data (Figures 1a and 1b). It is noted that the model simulates the climatological rainfall distribution over the continent reasonably well with a pattern correlation of 0.56, except that the rain shadow region over southeast India is rather small in the model simulation. This appears to be
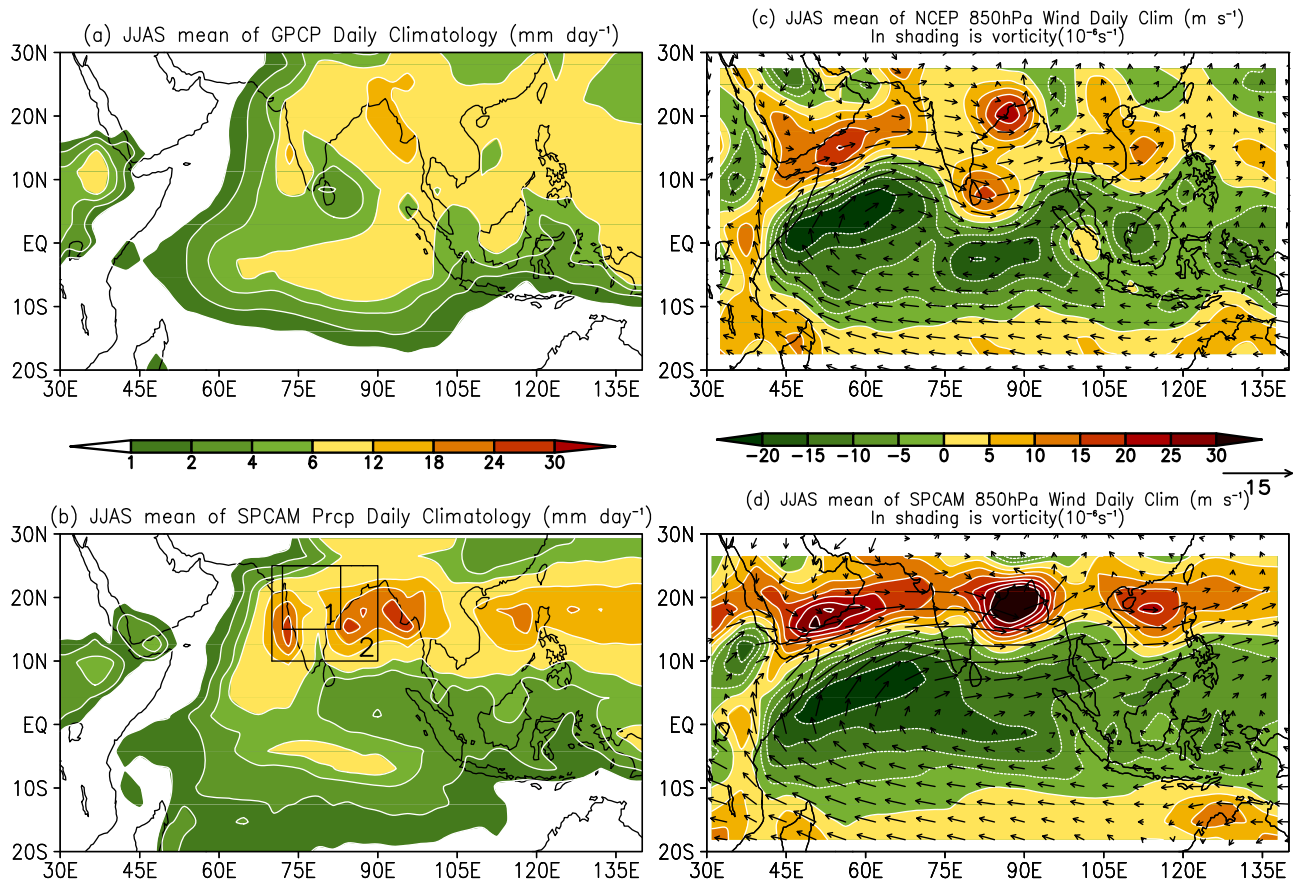
Figure 2. Climatological mean (JJAS) precipitation (mm d^{-1}) from (a) GPCP and (b) SP-CAM and 850 hPa winds (m s^{-1}) from (c) NCEP and (d) SP-CAM. In Figures 2c and 2d, the shaded area is the corresponding vorticity (10^{-6} s^{-1}), and the thick white line is the zero vorticity.

related to the inability of the climate model to resolve and simulate the amplitude of the Western Ghat precipitation. The amplitude of ISV as represented by the standard deviation of 10–90 day filtered rainfall anomalies simulated by the model within the continent is reasonable (Figures 1c and 1d) with a pattern correlation of 0.56, except that the model ISV is stronger than observed over east-central India and weaker than observed close to the Western Ghat.

[13] The Indian monsoon, however, is not confined within continental India and has a much larger spatial scale [*Webster et al.*, 1998]. To document the model biases in simulating the Indian monsoon on a larger scale, a comparison of the climatological mean JJAS precipitation in the SP-CAM and the observations using GPCP is made (Figure 2). While it indicates some similarities, a few important differences are noted. First, the northern rainband or the continental tropical convergence zone (TCZ) extends northward to about 20°N in both the SP-CAM simulations (Figure 2b) and observations (Figure 2a). Also, as in observations, the model simulates a maximum in precipitation in the equatorial Indian Ocean with a dry zone between the oceanic maximum or the oceanic TCZ and the continental TCZ. Furthermore, the oceanic TCZ is located in the eastern Indian Ocean as in observations. However, the SP-CAM simulation is far too wet in the regions of maximum precipitation compared to observations (Figure 2b). Also, it simulates an extra center of

high precipitation in the western Bay of Bengal (BoB), near the eastern coast of India at 15°N. Another feature of the simulation is that the northern rainband is too zonally oriented compared to the northeast-to-southwest orientation of the observed precipitation (Figure 2a).

[14] The strong wet bias and zonally oriented nature of simulated precipitation are also reflected in biases of the simulated JJAS climatological mean winds at 850 hPa (Figure 2d) compared to the observed climatology (Figure 2c). The low-level jet (LLJ) at 850 hPa is much stronger in the model than in observations, consistent with the model wet bias. Furthermore, consistent with the zonally oriented character of the simulated precipitation (Figure 2b), the winds associated with the LLJ are too zonally oriented, and strong zonal winds extend too far into the western Pacific. As a result, the climatological vorticity at 850 hPa simulated by the model is also too zonal and fails to simulate the cyclonic vorticity maximum in southeastern India (Figure 2c).

[15] In order to examine whether the model correctly simulates the onset and withdrawal of the monsoon and the time evolution of rainfall over the continent and near-coastal ocean, the annual cycle of daily climatological rainfall averaged over the two boxes in Figure 2b is computed (Figures 3a and 3b). The fluctuations in the daily climatology of rainfall from GPCP as well as from SP-CAM seen in Figures 3a and 3b are the climatological intraseasonal os-
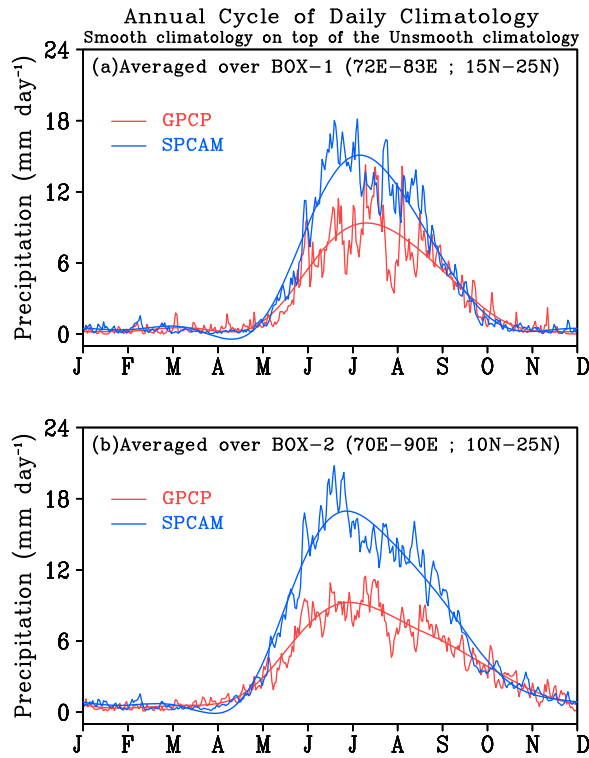
Figure 3. Seasonal evolution of rainfall (mm d^{-1}) over the two boxes, (a) Box-1 and (b) Box-2, shown in Figure 2b. Smoothed climatology is on top of unsmoothed daily climatology.
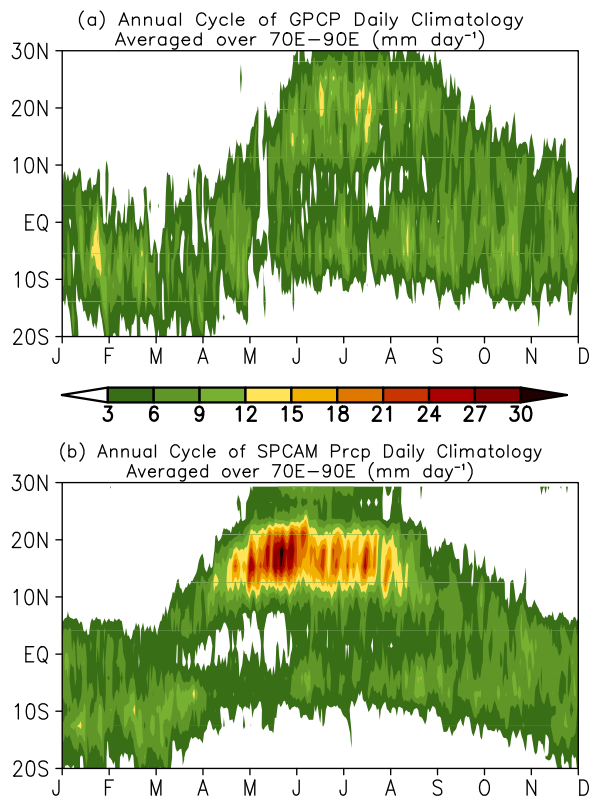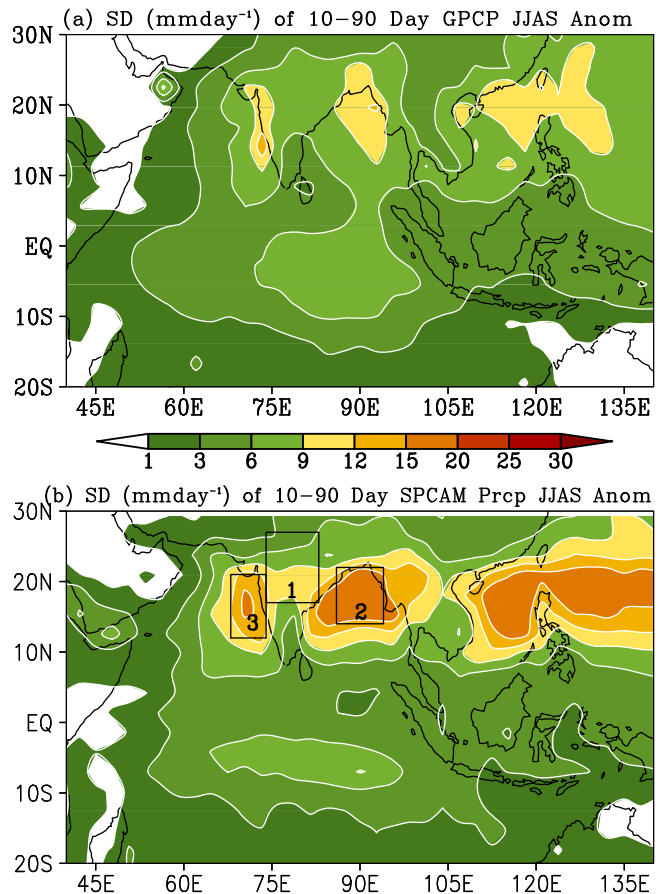

Figure 5. Standard deviation of 10–90 day bandpass-filtered daily precipitation (mm d^{-1}) anomalies (JJAS) from (a) GPCP and (b) SP-CAM. (The boxes in Figure 5b are plotted for Figures 15 and 16.)

Figure 4. Climatological annual cycle of precipitation over 70°–90°E (mm d^{-1}) from (a) GPCP and (b) SP-CAM.

cillations (CISO) [*Wang and Xu*, 1997]. However, because of the limited number of years (12) to create the climatology for GPCP, some sampling bias may be present in the GPCP CISO. The smoothed climatology constructed from the first three harmonics of the daily climatology and annual mean for both GPCP and SP-CAM are also shown in Figure 3. It is encouraging to note that the model simulates a rapid onset and a slow withdrawal of monsoonal precipitation as observed [*Krishna Kumar et al.*, 2011]. The timing of these onsets and withdrawals are similar to observations, with a rapid increase in climatological precipitation during May and gradual decline during August and September. A simulated wet bias persists throughout the summer monsoon season, however. It is also encouraging to note that during the winter season, the simulated rainfall is near zero as in observations. The annual cycle and northward migration of the TCZ is explored by plotting simulated daily climatological precipitation averaged from 70°E and 90°E as a function of latitude and time (Figure 4b) compared to observations (Figure 4a). It is noted that the model shows promise in simulating the double TCZ in the monsoon domain (Figure 4b), one over the Indian subcontinent and the other over the Indian Ocean, owing to a reasonable northward propagation of the TCZ. The model, however, shows a wet bias over the
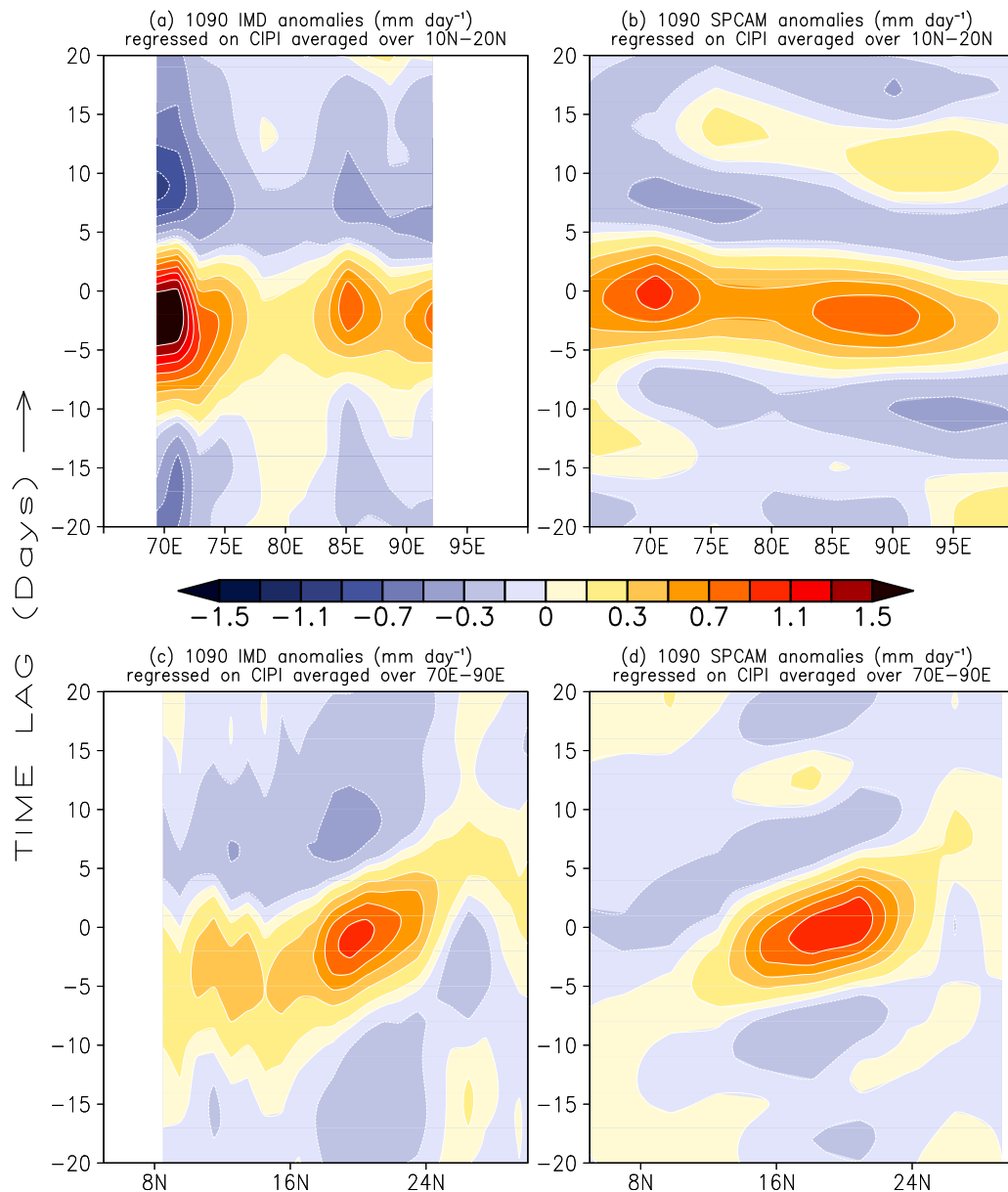
Figure 6. (a) Longitude-time and (c) latitude-time plots of 10–90 day filtered IMD anomalies regressed on CIPI, averaged over 10°–20°N and 70°–90°E, respectively. (b and d) Same as Figures 6a and 6c but for SP-CAM output.

continental branch of the TCZ, which increases in amplitude earlier than observations (Figure 4a).

4. Simulation of Monsoon Intraseasonal Variability

[16] The space-time characteristics of simulated monsoon intraseasonal variability are examined in this section and compared with those of the observed variability. We define the amplitude of ISV as the standard deviation of the 10–90 day bandpass-filtered daily precipitation anomaly during June–September. Model variability (Figure 5b) is compared to that from observations (Figure 5a). The spatial patterns of precipitation ISV in observation and the model (Figure 5) are similar to the climatological seasonal mean precipitation

(Figure 2a). This relationship between the mean and variance appears to be consistent with the fact that observed and simulated precipitation follows a Poisson distribution (figure not shown) for which variance is proportional to the mean. Thus, compared to observations, the stronger ISV simulated by the model is consistent with its large wet bias in the simulation of seasonal mean precipitation.

[17] A quick assessment of the model's ability to simulate the eastward and northward propagation characteristics of summer ISV over the Indian continent is done in Figure 6. This is based on lag regressions of 10–90 day filtered precipitation with respect to a reference time series of 10–90 day filtered precipitation averaged over central India. It is seen that within the continental India, the model simulates the eastward (Figure 6b) and northward (Figure 6d) propagation
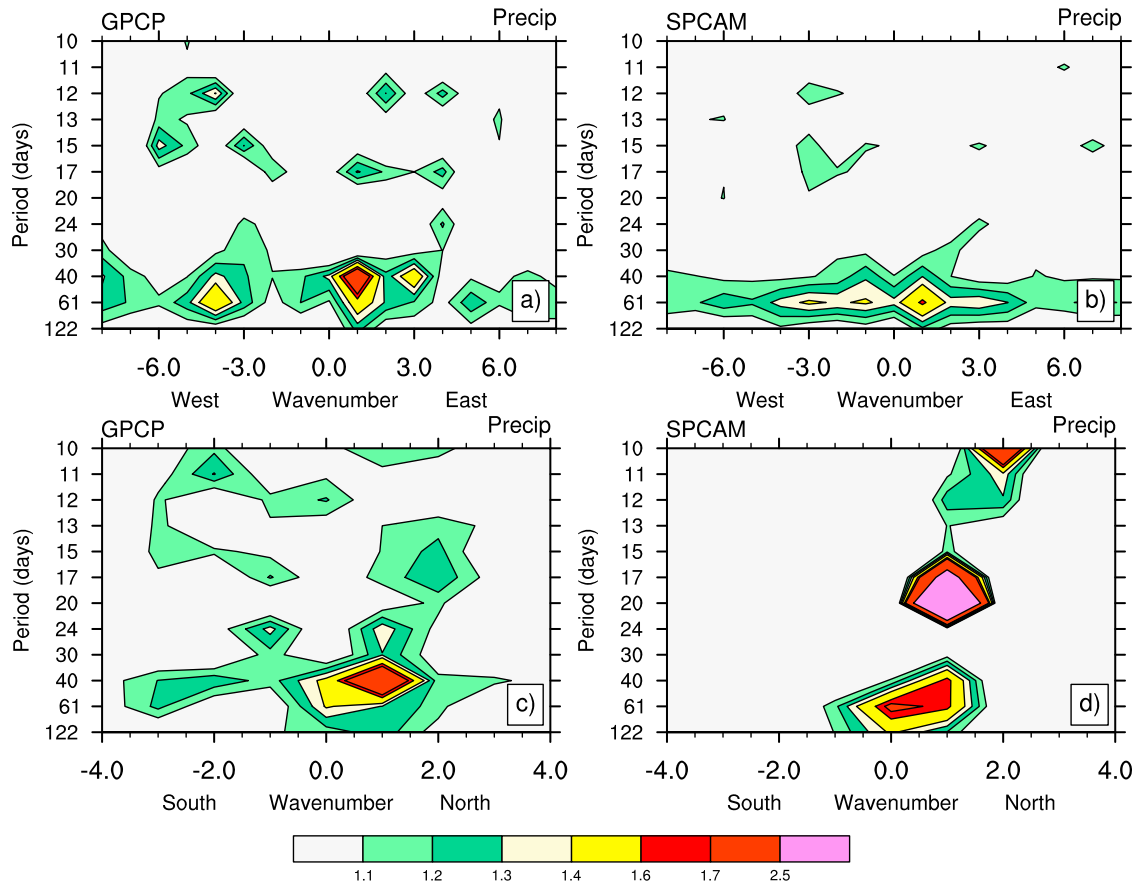
Figure 7. Wave number-frequency power spectra of precipitation. Zonal power spectra (divided by the background) calculated over 0°–360°, 15°S–15°N for (a) GPCP precipitation and (b) model-simulated precipitation. Meridional power spectra calculated over 15°S–30°N, 60°–110°E for (c) GPCP precipitation and (d) model-simulated precipitation.

reasonably well compared to IMD observations (Figures 6a and 6c). However, it is consistent with earlier discussions of the model's inability to simulate the observed high ISV in the Western Ghat region (Figures 6a and 6b).

[18] In order to examine the model's fidelity in simulating the dominant modes of ISV during northern summer, space-time spectra of daily precipitation from GPCP and from the SP-CAM are calculated following the methodology of *Wheeler and Kiladis* [1999]. The daily anomalies from the JJAS period for all 12 available years of GPCP and a similar 12 years of data from the SP-CAM are used in the spectral calculations. Space-time spectra are calculated for zonally propagating modes using global data at each latitude and then averaging the resulting power between 20°S and 30°N. These spectra are shown for GPCP (Figure 7a) and the model (Figure 7b). Similarly, space-time spectra for meridional propagation are calculated using data between 20°S and 30°N and then averaging the spectral power between 60°E and 135°E. These spectra are shown in Figure 7c from GPCP and in Figure 7d from the model. In calculating the space-time spectra for meridional propagation, the choice of the domain bounds is based on the fact that the northward propagating MISO is generally confined between 20°S and 30°N within this domain [see *Goswami*, 2005]. Meridional wave number 1 is defined on the basis of the largest wave that entirely fits inside the domain. In

interpreting these spectra, it must be kept in mind that the domain is not periodic and hence some artificial spectral power may be introduced into the wave number-frequency spectrum. However, sensitivity tests indicate that the location and power of the dominant spectral signals are insensitive to modest changes in the domain size.

[19] The spectra indicate the following behavior.

[20] 1. The model simulates the eastward propagating mode at wave number 1 with a longer period (60 days) than in observations (45 days). With significant power at westward propagating wave number 1, the simulated mode may have a stationary component, although we would need to conduct an analysis of coherence between eastward and westward components to confirm this.

[21] 2. In observations, the dominant northward propagating mode appears to be the same 45 day eastward propagating mode (Figures 7a and 7c). However, in the model, the dominant northward propagating mode is a 20 day mode with no zonal propagating counterpart (Figures 7b and 7d). The simulated 60 day mode, in addition to having a meridional structure with meridional wave number 1, has a significant power in meridional mean component.

[22] Thus, in addition to simulating the observed 45 day mode with a longer period of 60 days, the model's dominant northward propagating mode in the region is a 20 day mode. A question that can be raised is the degree to which this new
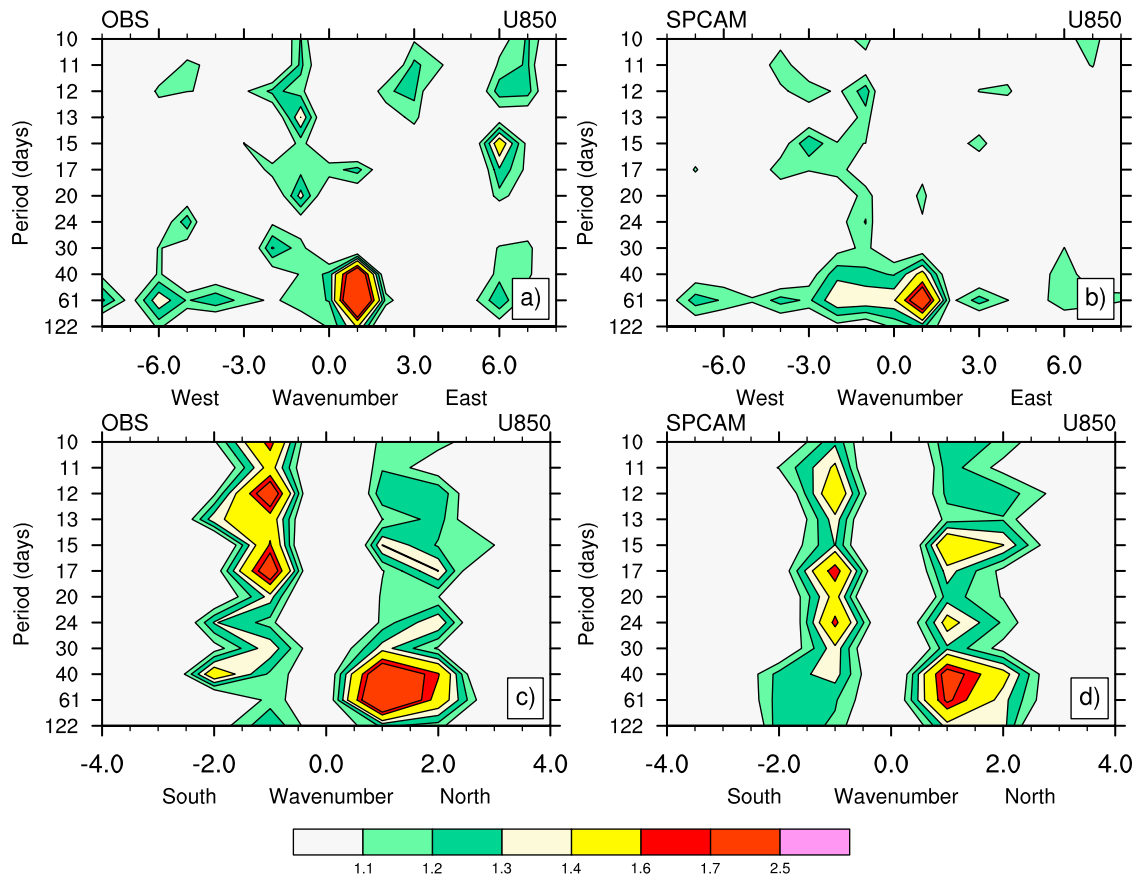
Figure 8. Wave number-frequency power spectra of zonal wind at 850 Mb. Zonal power spectra calculated over 0°–360°, 15°S–15°N for (a) NCEP/NCAR reanalysis U wind and (b) model-simulated U wind. Meridional power spectra calculated over 15°S–30°N, 60°–110°E for (c) NCEP/NCAR reanalysis U wind and (d) model-simulated U wind.
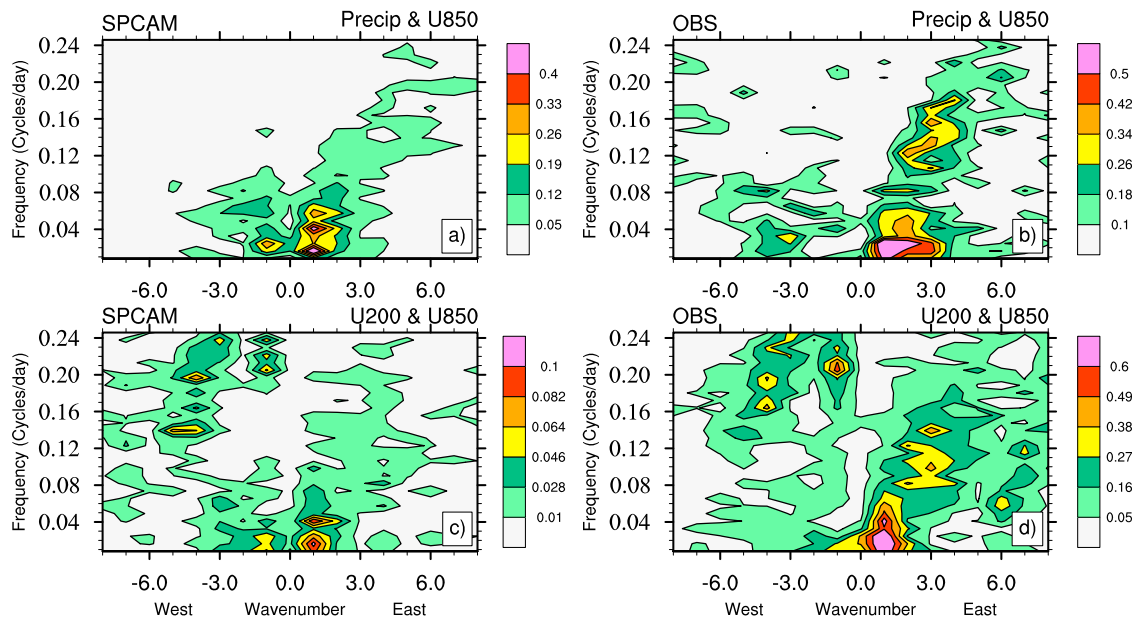

Figure 9. Space-time coherence squared spectrum for symmetric latitudes 15°S–15°N: (a) model-simulated precipitation with zonal wind at 850 hPa; (b) GPCP precipitation with NCEP/NCAR reanalysis wind at 850 hPa; (c) model-simulated zonal wind at 200 hPa with zonal wind at 850 hPa; and (d) NCEP/NCAR reanalysis zonal wind at 200 hPa with that at 850 hPa.
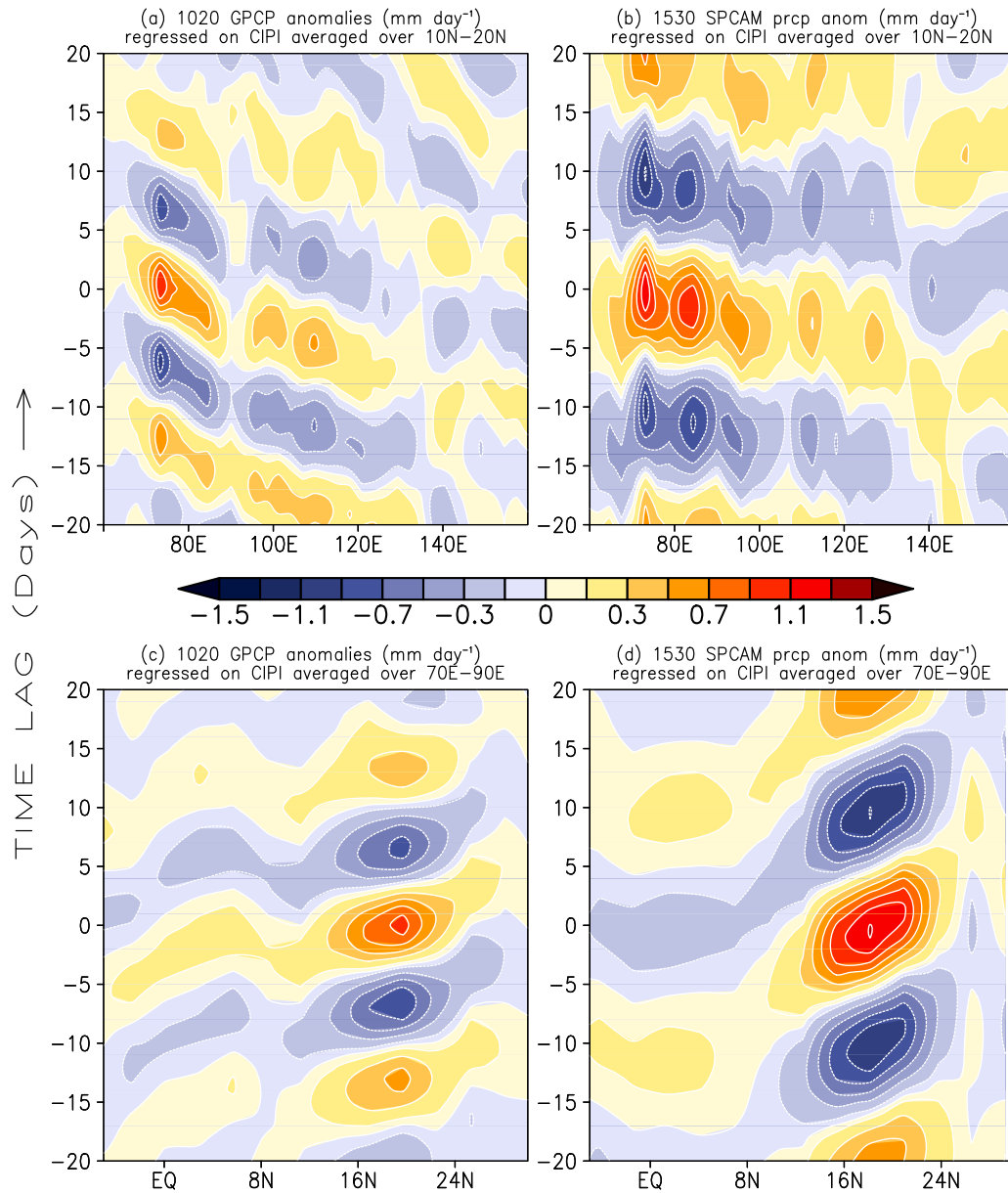
Figure 10. (a) Longitude-time and (c) latitude-time plots of 10–20 day filtered GPCP anomalies regressed on CIPI, averaged over 10°–20°N and 70°–90°E, respectively. (b and d) Same as Figures 10a and 10c but for SP-CAM output with 15–30 day filter.

model mode exhibits coherence between convection and the large-scale circulation. Comparing the space time spectra of daily 850 hPa (JJAS) winds simulated by SP-CAM with the space-time spectra of observed winds (Figure 8), we find that the meridional propagating component of the simulated 60 day mode exhibits coincident peaks in wind and precipitation, indicating strong coupling between convection and the large-scale circulation. While the simulated 20 day mode in precipitation (Figure 7d) clearly exhibits northward propagation, near the same periods in low-level winds, a significant stationary component is indicated (Figure 8d) with comparable power in both northward and southward wave number bands.

[23] To gain further insight into the covariability of the model convection and circulation fields in the spectral domain, the coherence squared spectra between symmetric precipitation and winds were estimated using the daily anomalies. The coherence squared spectrum is obtained by normalizing the cross-power spectrum that contains both magnitude and phase of the relationship between the two fields, with the individual powers in each field [*Hendon and Wheeler*, 2008]. It can be interpreted as the wave number-frequency distribution of the squared correlation coefficient between the two fields. The coherence squared spectra between the SP-CAM symmetric precipitation and daily wind fields at 850 hPa (Figure 9a) shows a peak coherence squared of 0.4 coherence associated with the MJO that is weaker than the coherence exhibited by GPCP precipitation and NCEP winds at 850 hPa (Figure 9b). The model symmetric precipitation and 200 hPa wind fields show very high
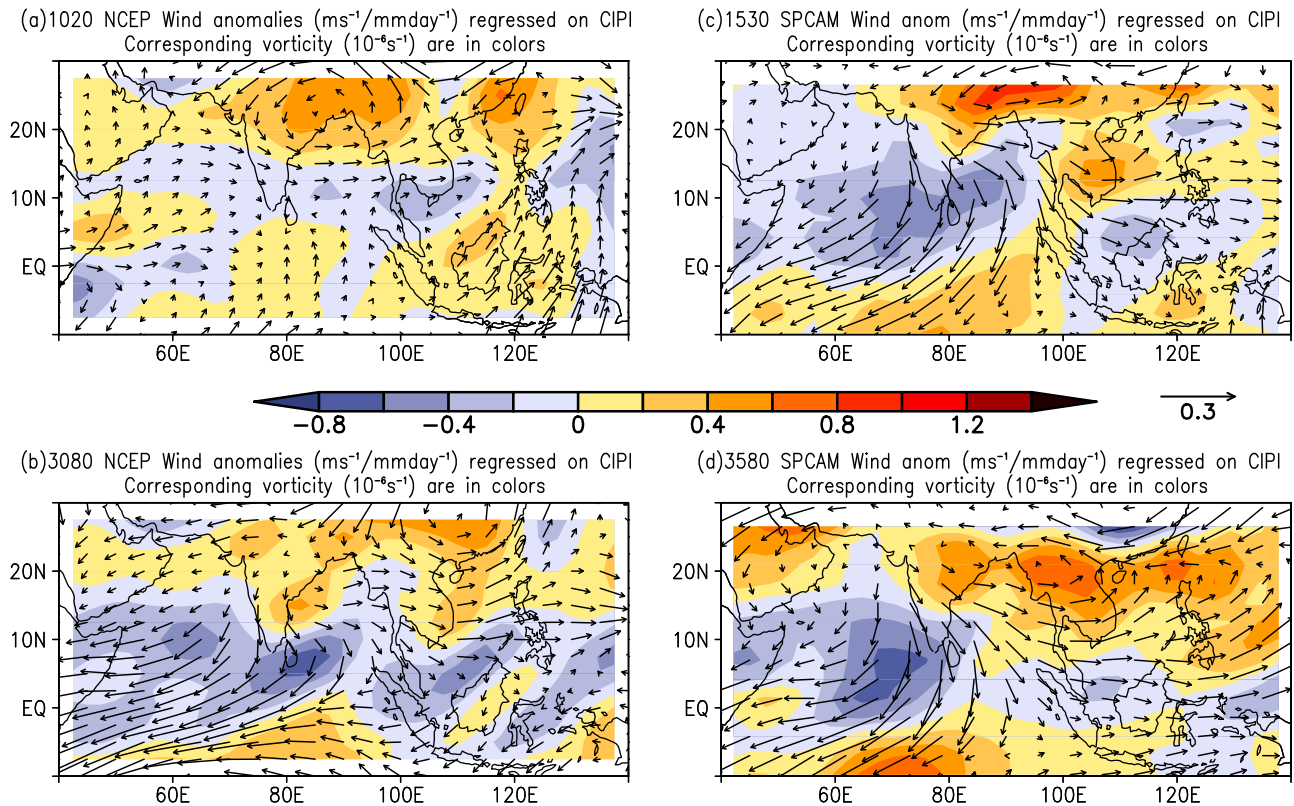
Figure 11. Filtered 200 hPa wind anomalies regressed on CIPI: (a) 10–20 day filtered NCEP; (b) 30–80 day filtered NCEP; (c) 15–30 day filtered SP-CAM; and (d) 35–80 day filtered SP-CAM. Vorticity anomalies are in colors.

coherence corresponding to the MJO (not shown). While the observed precipitation field (GPCP) exhibits strong coherence with both lower and upper level circulation, the model precipitation field is more strongly coupled with the upper level winds, indicating a bias in the vertical wind structure. The small coherence squared spectra of 200 and 850 hPa symmetric model winds in the MJO band (Figure 9c) also corroborates this notion, in contrast to the strong correlation between upper and lower level winds seen in observations (Figure 9d).

5. Diagnosis of the Simulated Modes

[24] Observed monsoon intraseasonal variability consists of a well-documented quasi-biweekly mode (or a 15 day mode) as described in many studies and a mode centered on 45 days (for a review, see *Goswami* [2005]). These modes have distinct horizontal and vertical structures and propagation characteristics. The simulated 20 and 60 day modes do not occupy the same place in the space-time spectra as the observed modes, and so it is important to identify to what extent the model modes are dynamically distinct from the observed modes and what the simulated modes represent. For example, is the simulated 20 day mode similar to the observed 15 day mode, and is the simulated 60 day mode simply a model version of the observed 45 day mode?

5.1. The 20 Day Mode

[25] We first compare horizontal and vertical structure and propagation characteristics of the simulated 20 day mode and the observed 15 day mode. For this purpose, the simulated 20 day mode in precipitation and winds is isolated using a 15–30 day Lanczos filter [*Duchon*, 1979]. The observed 15 day mode is isolated by using a 10–20 day Lanczos filter on GPCP daily precipitation and NCEP wind anomalies. We use lag-regression techniques to illustrate propagation characteristics of these modes for which a reference time series is needed [*Wilks*, 1995]. A reference precipitation time series for use in regression is created by averaging filtered anomalies over central India between 15°–25°N, 73°–82°E where the amplitude of variability is large both in observation and in model simulation. We then lag regress filtered anomalies for the entire map on to the reference time series. The zonal propagation of the respective modes is illustrated in Figures 8a and 8b, where regression coefficients averaged between 10°N and 20°N are plotted. Similarly, north-south propagation is illustrated in Figures 10c and 10d where the regressed values averaged between 70°E and 90°E are plotted. While the observed 15 day mode has clear westward propagation (Figure 10a), the simulated 20 day mode is relatively stationary in the east-west direction (Figure 10b). Although there seems to be two discontinuous precipitation regimes, one east of 100°E and another west of this line, in both the regimes, the simulated mode does not have a strong propagating character.
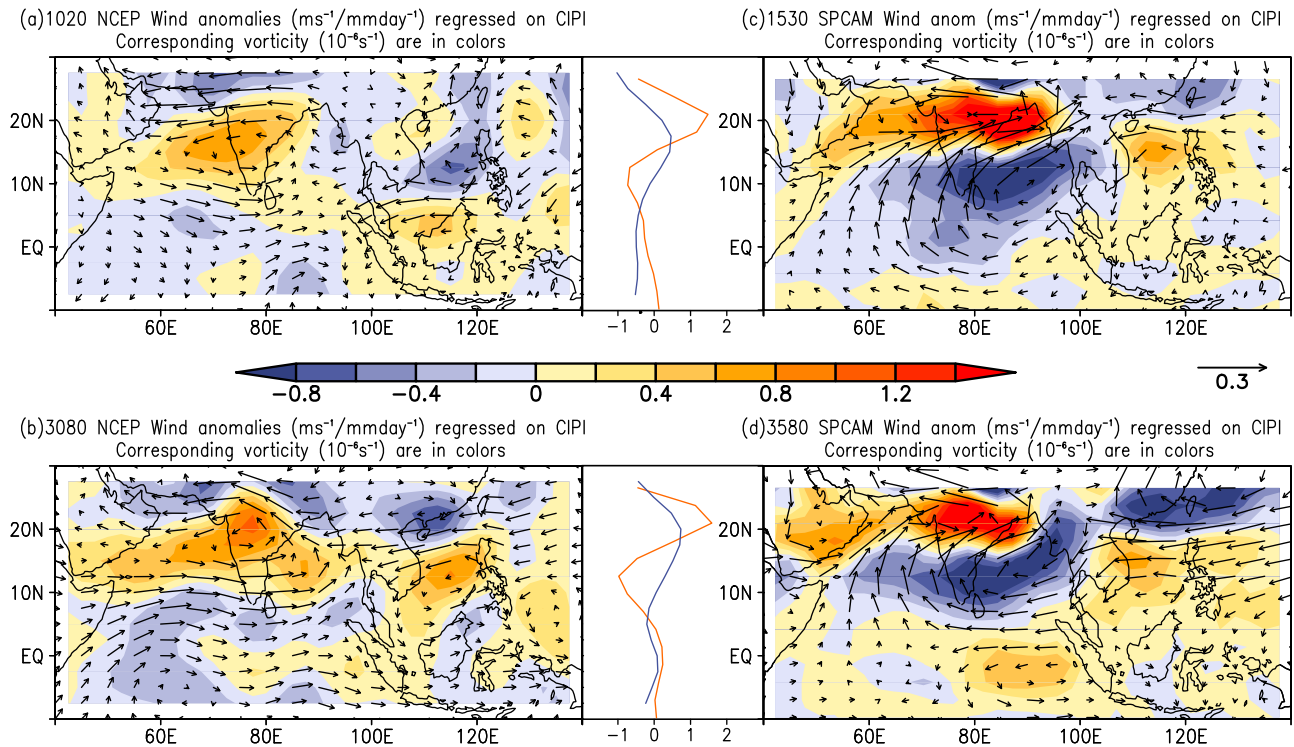
GOSWAMI ET AL.: MISO AND SP-CAM

Figure 12. Filtered 850 hPa wind anomalies regressed on CIPI: (a) 10–20 day filtered NCEP; (b) 30–80 day filtered NCEP; (c) 15–30 day filtered SP-CAM; and (d) 35–80 day filtered SP-CAM. The corresponding vorticity (10^{-6} s^{-1}) is plotted in the background (shading). Line plots (middle top and bottom) are correspondingly filtered regressed vorticity (10^{-6} s^{-1}) averaged over 70°–85°E; the blue line represents NCEP output, and the red line represents SP-CAM output.

Similarly, while the observed 15 day mode is relatively stationary in the north-south direction (Figure 10c), the simulated 20 day mode is clearly northward propagating at a rate of about 1.2° d^{-1} (Figure 10d).

[26] In order to gain insight into the vertical structure of the simulated 20 day mode and compare it with the vertical structure of the observed 15 day mode, filtered wind anomalies are regressed onto the filtered central India precipitation index (CIPI). The regressed wind patterns for the observed 15 day mode (Figures 11a and 12a) show that the 850 hPa cyclonic anomaly pattern (Figure 12a) also extends up to 200 hPa (Figure 11a). This barotropic vertical structure of the observed 15 day mode is consistent with earlier studies [*Chatterjee and Goswami*, 2004]. For the simulated 20 day mode, however, the cyclonic and convergent 850 hPa circulation (Figure 12c) is overlaid by a divergent anticyclonic circulation pattern at 200 hPa (Figure 11c), indicating that together with a barotropic component, a baroclinic component may be present in the vertical structure. A more detailed examination of the vertical structure associated with the mode (see Figure 14b) also supports this conclusion.

[27] Although the period of the simulated 20 day mode is close to that of the observed 15 day mode, the vertical structure and propagation characteristics of the mode suggest that it is distinctly different from the observed 15 day mode. Thus, it may be inferred that the simulated 20 day model is a new model-generated mode that is not observed.

5.2. The 60 Day Mode

[28] The simulated 60 day mode, as well as the observed 45 day mode in precipitation and winds, is isolated using a 30–80 day (for observation) and a 35–80 day (for simulation) Lanczos filter. A reference time series is created by averaging filtered anomalies over central India between 15°–25°N, 73°–82°E for GPCP and for the model-simulated rainfall. Lag regressions of the filtered anomalies are then calculated with respect to the reference time series. The zonal propagation of the mode is illustrated in Figures 13a and 13b where regressed values averaged between 10°N and 20°N are plotted. Similarly, meridional propagation is illustrated in Figures 13c and 13d where the regressed values averaged between 70°E and 90°E are plotted. Furthermore, while the observed 45 day mode has a clear eastward propagation (Figure 13a), the simulated 60 day mode has only a weak eastward propagation between 60°E and 120°E (Figure 13b). Similarly, while the observed 45 day mode has a clear northward propagation with speed of about 1.1° lat d^{-1} (Figure 13c), the simulated 60 day mode exhibits much slower northward propagation at a rate of about 0.5° lat d^{-1} (Figure 13d).

[29] Filtered wind anomalies are regressed against the filtered precipitation index averaged over central India (10°–20°N, 70°–90°E) to examine the vertical structure of the simulated and observed modes. The regressed wind patterns for the observed 45 day mode (Figure 12b) show that the 850 hPa cyclonic and convergent pattern of anomaly is
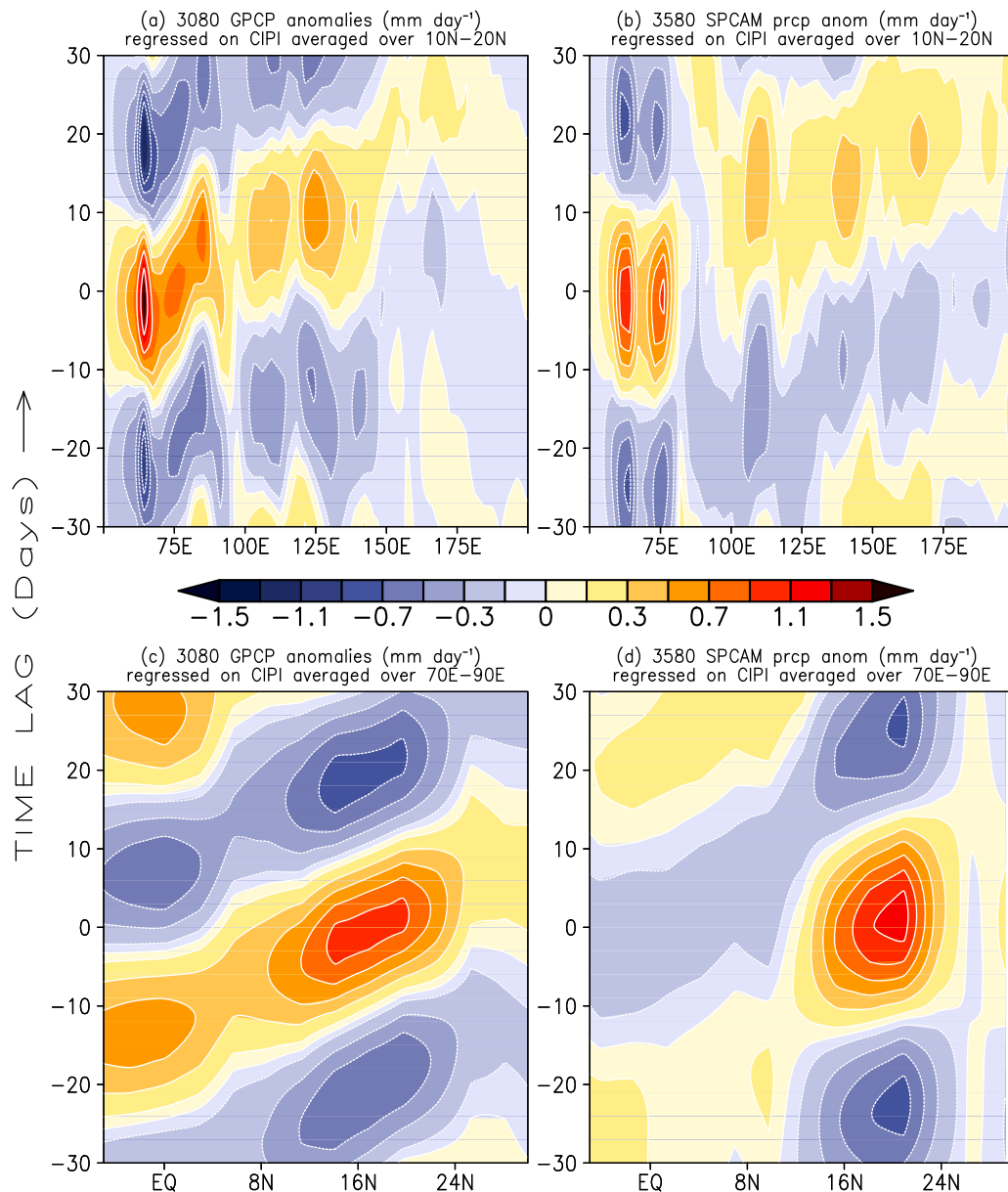
Figure 13. (a) Longitude-time and (c) latitude-time plots of 30–80 day filtered GPCP anomalies regressed on CIPI, averaged over 10°–20°N and 70°–90°E, respectively. (b and d) Same as Figures 13a and 13c but for SP-CAM output with 35–80 day filter.

overlaid by a divergent anticyclonic anomaly pattern at 200 hPa (Figure 11b). The simulated 60 day mode also demonstrates a similar cyclonic and convergent 850 hPa circulation overlaid by a divergent anticyclonic circulation pattern at 200 hPa (Figures 12d and 11d).

[30] Both the observed 45 day mode and the simulated 60 day mode have a similar dominant baroclinic component in the vertical structure and time scale. Thus, the simulated 60 day mode seems to be the model version of the observed 45 day mode. Comparing Figures 12b and 12d, we find that the horizontal scale of simulated 60 day mode (red line) is smaller than that of the observed 45 day mode (blue line). It can also be noted that the simulated regressed wind field at the 20 day mode (Figure 12c) resembles that of the simulated 60 day mode (Figure 12d), particularly over the monsoon region.

5.3. On the Northward Propagation

[31] It has been suggested that the northward propagation of the observed 45 day mode is a result of a feedback between convective heating and circulation [e.g., *Jiang et al.*, 2004]. In the presence of an easterly shear of background winds, the atmospheric response to a heating anomaly produces a barotropic cyclonic vorticity center and anomalous lower tropospheric moisture convergence to the north of the heating maximum. This helps the heating anomaly to propagate northward. To examine the model's fidelity in simulating this process, bandpass-filtered vorticity anomalies are composited relative to OLR anomalies
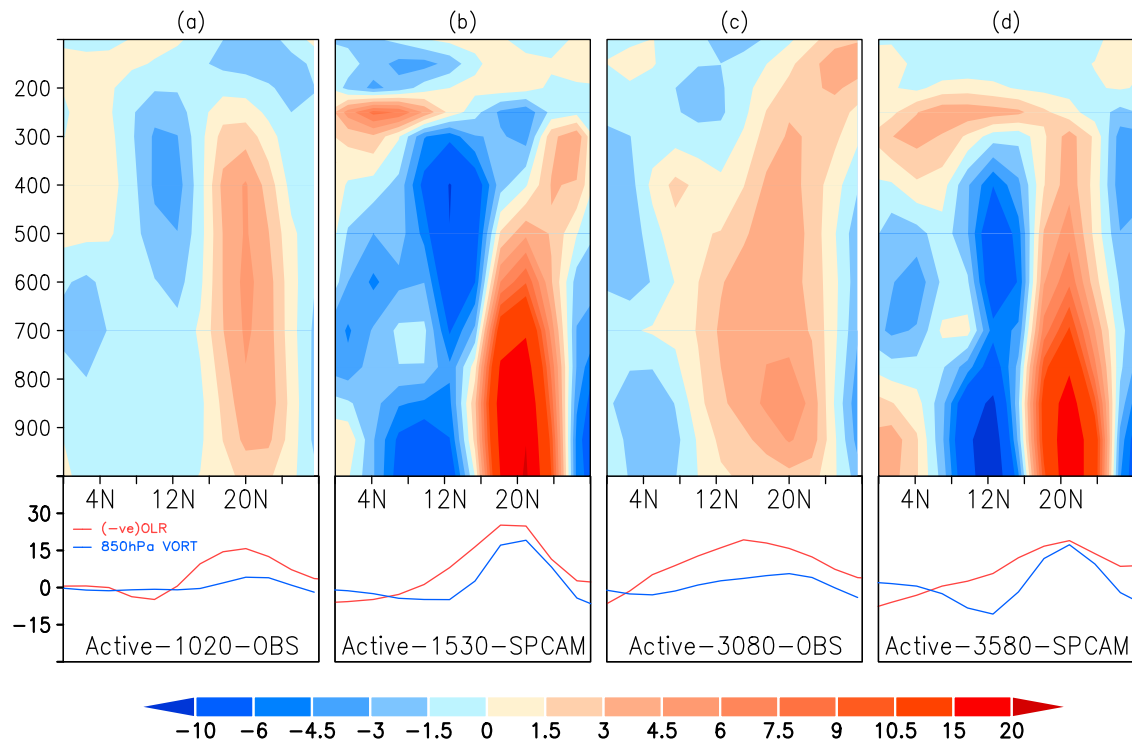
Figure 14. Composite of vorticity (5×10^{-6} s^{-1}) anomaly averaged over 70°–90°E, for the active monsoon condition, for observed data (NCEP) with (a) 10–20 day filter and (c) 30–80 day filter and for SP-CAM output with (b) 15–30 day filter and (d) 35–80 day filter. Corresponding OLR (Wm^{-2}) (red line) and 850 hPa vorticity (blue line) composites are plotted at the bottom.

corresponding to active spells, defined using minima of filtered OLR averaged over central India (15°–25°N, 73°–82°E). The vertical structure of the vorticity anomalies for the simulated 20 and 60 day modes averaged between 70°E and 90°E are shown in Figures 14b and 14d as a function of latitude. Similar composites of vorticity anomaly for the observed 15 day mode and the 45 day mode are shown in Figures 14a and 14c. The composite OLR for each mode averaged between 70°E and 90°E are also shown below each vorticity plot, in addition to the anomalous 850 hPa vorticity. It is noted that the minimum of OLR (convection maximum) for the observed 15 day mode is nearly collocated with the location of the barotropic vorticity maximum (Figure 14a, top and bottom), consistent with the lack of northward propagation in this case as in the theory of *Jiang et al.* [2004]. However, the low-level cyclonic vorticity maximum for the model 20 day mode is slightly shifted north of the OLR minimum (Figure 14b, top and bottom), consistent with the northward propagation of this mode. Consistent with Figures 12c and 11c, in the case of the simulated 20 day mode, the center of low-level cyclonic vorticity is overlaid by an anomalous anticyclonic circulation in the upper troposphere, indicating the baroclinic nature of the vertical structure.

[32] In the case of the simulated 60 day mode (Figure 14d, top and bottom), however, the low-level vorticity maximum is nearly collocated with the OLR minimum, consistent with a weak northward propagation or a nearly stationary character of this mode in the north-south direction (Figure 13d). For the observed 45 day mode (Figure 14c, top and bottom),

the cyclonic vorticity maximum is located north of the OLR minimum, as expected.

6. Diagnostic of Seasonal Mean Bias

6.1. Simulated Probability Distribution of Daily Rainfall and the Seasonal Mean Bias

[33] The analyses in the earlier sections have brought out the wet bias of the model compared to observation based on daily rainfall climatology. As the mean and variance of rainfall distribution are linearly related, it is possible that the bias in simulating the mean rainfall may be related to biases in simulating the frequency distribution of rain rates. Three representative areas over central India (Figure 5b, box 1), Bay of Bengal (Figure 5b, box 2), and Arabian Sea (Figure 5b, box 3) are chosen, and the probability distribution function (PDF) in percentage is computed for different rain rate categories, based on daily rainfall with a bin width of 5 mm. The PDF over central India (Figure 15a) reveals that the model underestimates the probability of occurrence of lighter rain rates and overestimates the moderate rain rates. The observations over Bay of Bengal (Figure 15b) and Arabian Sea (Figure 15c) show that lighter rain rate categories dominate, which the model is not able to capture. The model rain rates are shifted toward moderate and heavy categories over both the oceanic basins. Thus, the model shows a tendency for simulating heavy rain events with higher frequency over oceanic regions and also, to a certain extent, over Central India and fails to simulate the lighter rainfall categories with the same frequency as in the
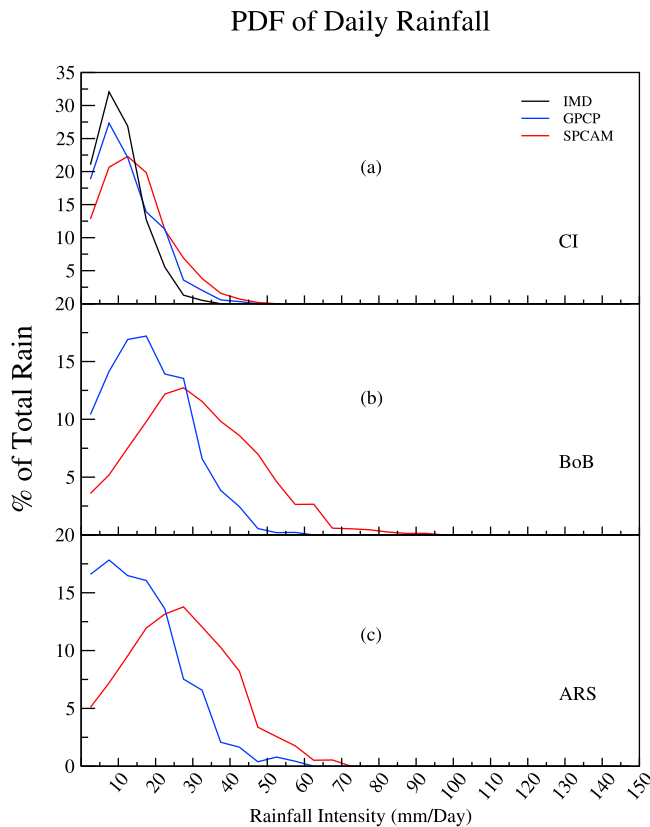
PDF of Daily Rainfall

Figure 15. Probability distribution function in percentage for (a) central India, (b) Bay of Bengal, and (c) Arabian Sea (the boxes are shown in Figure 5b), based on daily rainfall (mm d^{-1})with a bin width of 5 mm.

observations. These biases explain the wet bias in the simulation of the seasonal mean rainfall.

6.2. Vertical Structure of Rain Events and Seasonal Mean Bias

[34] The above analyses clearly demonstrate the model tendency of generating more heavy rainfall events, which seems to suggest too frequent deep convection. Thus, a natural question is what could be the possible source of such model bias? To find an answer to this question, we want to further quantify the possible source of such model behavior by analyzing the vertical structure of heating.

[35] A significant fraction of monsoon interannual variability (IAV) in observations as well as in models arise from "internal dynamics" and appears to owe its origin to the intraseasonal oscillations [*Goswami*, 1998; *Ajaya Mohan and Goswami*, 2003; *Goswami and Xavier*, 2005]. Monsoon intraseasonal oscillations (ISOs) may influence the seasonal mean monsoon through two different mechanisms. As the spatial structure of the dominant MISO has a significant projection on the dominant mode of IAV of the monsoon, an asymmetry in the frequency of occurrence of active and break spells can lead to a bias of the seasonal mean ISO anomalies leading to a contribution to the seasonal mean [*Goswami et al.*, 2006]. However, this linear mechanism cannot explain the total internal IAV simulated by a model [*Goswami and Xavier*, 2005]. Also, the nonlinear relationship between area averaged variance of ISO

anomalies and IAV of seasonal mean monsoon [*Goswami and Xavier*, 2005] indicate that there exists a nonlinear mechanism through which the MISO could influence the seasonal mean. Therefore, it is reasonable to think that biases of a model in simulating the seasonal mean monsoon may be linked to the biases of the model in representing the MISO.

[36] From Figure 14, we note that the simulated cyclonic vorticity anomalies associated with active phases of both the lower- and higher-frequency modes are more than three times stronger than the observed anomalies. In particular, the cyclonic vorticity anomalies associated with the simulated 20 day mode are even stronger than those for the simulated 60 day mode. Therefore, the simulated 20 day mode not only dominates the ISV, it may also influence the seasonal mean. Another interesting feature about the vertical structure of the vorticity anomaly associated with the two simulated modes is that unlike the observed modes where the maximum of vorticity anomaly tends to occur aloft, the maximum vorticity anomalies for the simulated modes occur very near the surface (Figure 14).

[37] The low-level cyclonic vorticity simulated by the model produces strong low-level moisture convergence and leads to the positive precipitation bias of the model (see Figure 2). As mentioned earlier, since the ISOs can influence the seasonal mean, a strong 20 day mode in the model with its associated strong vorticity may be a leading contributor to strong low-level moisture convergence and the mean precipitation bias of the model. Therefore, it is important to understand why the vorticity anomalies in the simulated modes are generally much stronger than those observed and why it is particularly strong in the 20 day mode. One possibility is that the meridional scale of the simulated modes is significantly smaller than that of the observed modes (see Figure 13), leading to a much stronger meridional gradient of zonal wind anomalies and stronger vorticity anomaly. Figure 14b suggests that the vertical structure of vorticity anomalies associated with the 20 day simulated mode is characterized by a higher-order baroclinic component that makes it more complex than the observed mode. Dynamically, if the simulated mode is associated with a higher-order baroclinic structure compared to observations, it would also be associated with a smaller horizontal scale [*Pedlosky and Frenzen*, 1980]. This can happen if the heating profile produced by the model has a strong maximum in the upper troposphere (200–300 hPa), and if that maximum is much stronger in the case of the 20 day mode compared to the 60 day mode. To gain some insight on this issue, we examined the vertical profiles of CRM heating tendencies for the two modes over three representative regions shown in Figure 5b. The composite vertical profile of CRM heating tendency for 15–30 and 35–80 day filtered data during active phases over different subregions is shown in Figure 16. The vertical profile of heating tendency for active periods is found to have sharper vertical structure for the 15–30 day mode over the BoB (Figure 16b, red line), Western Ghat (Figure 16c, red line), and central Indian (Figure 16a, red line) regions compared to the 35–80 day mode (Figure 16, blue line). Similar differences in the vertical profile of CRM heating tendency are also noted between 15 and 30 day and 35–80 day modes during breaks (not shown). It is also noted that the maximum heating rates
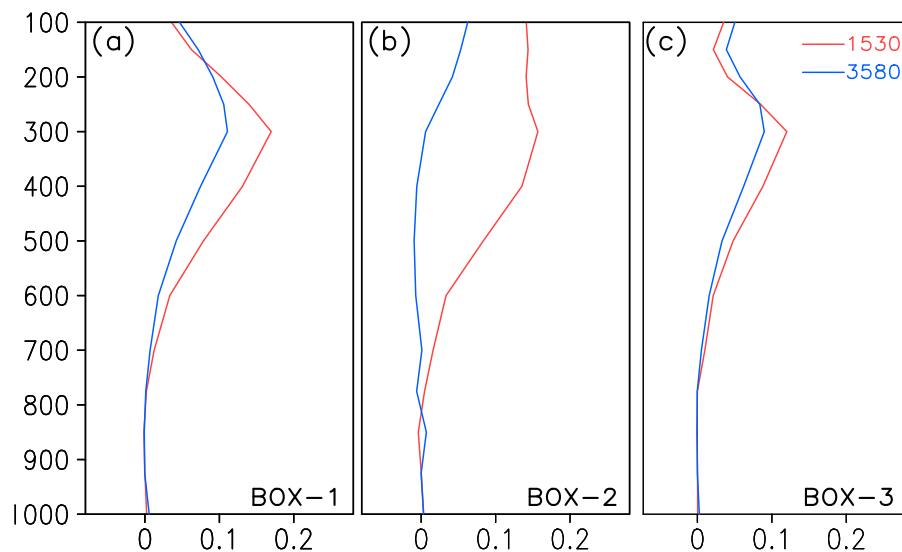
Figure 16. Composite 15–30 (red line) and 35–80 (blue lines) day filtered vertical heating tendency (10^{-4} K s^{-1}) of the CRM, in MMF, for active monsoon conditions averaged over the boxes shown in Figure 5b.

are in the upper troposphere between 200 and 300 hPa. The CRM heating tendencies are stronger in the 15–30 day mode, and, as a response, the SP-CAM shows enhanced upper (lower) level divergence (convergence), which adds to the larger precipitation bias in the 15–30 day mode compared to the 35–80 day mode, although depending on the energetics of the system, the large-scale circulation biases may simply be a response to the precipitation bias rather than a cause.

7. Conclusions

[38] Realistic simulation of the observed space-time characteristics of MISOs is important for a model's ability to simulate the seasonal mean with fidelity. In the present study, we examine simulation of seasonal mean boreal summer monsoon characteristics and MISOs from a 20 year SP-CAM AMIP style forced by observed sea surface temperatures. The SP-CAM has a reasonable seasonal cycle of the Indian monsoon. However, the model shows a strong wet bias during northern summer over the Asian monsoon region. A similar wet bias in Asian summer monsoon simulation by SP-CAM was found by *Luo and Stephens* [2006], which they had attributed to the periodic boundary condition of the CRMs. An attempt is made to diagnose the cause of this wet bias in the model simulations.

[39] The model shows limited ability to capture observed intraseasonal modes with fidelity. The model simulates an eastward propagating mode of wave number 1 with a longer period (60 days) compared to observations (45 days). The simulated mode also appears to have significant power at westward propagating wave number 1, suggesting a stationary component compared to observations. While the vertical structure of the simulated mode is similar to the observed 45 day mode, its northward propagation is much slower than its observed counterpart.

[40] The model does not realistically simulate the observed quasi-biweekly mode. Instead, it produces a very strong 20 day mode with robust northward propagation. The simulated 20 day mode has a baroclinic component in the vertical structure in contrast to the observed 10–20 day mode, which has a strong barotropic component. Thus, the 20 day simulated mode shows no observational analog and may hold a key for understanding its seasonal mean precipitation bias in the model.

[41] The strong northward propagation of the simulated 20 day mode is associated with strong cyclonic vorticity produced at low levels to the north of the heating maximum, consistent with the hypothesis of *Jiang et al.* [2004]. Strong vorticity associated with the mode, in turn, is associated with a smaller meridional scale of the simulated mode. As the circulation response depends crucially on the vertical structure of convective heating, we examined the CRM heating rates within the SP-CAM. Analysis of the vertical structure of the SP-CAM heating rates indicates that it produces a strong heating maximum in the upper atmosphere between 200 and 300 hPa. Such a heating profile would tend to support a higher-order baroclinic mode response (second baroclinic mode or higher). Higher-order baroclinic modes are generally associated with a smaller meridional structure, stronger low-level cyclonic vorticity, stronger low-level moisture convergence, and higher precipitation. The vertical structure of heating simulated by the CRM within SP-CAM may therefore hold a key for improving the wet bias of summer simulation of the model.

References

Ajaya Mohan, R. S., and B. N. Goswami (2003), Potential predictability of the Asian summer monsoon on monthly and seasonal time scales, *Meteorol. Atmos. Phys.*, *84*, 83–100, doi:10.1007/s00703-002-0576-4.

Benedict, J. J., and D. A. Randall (2009), Structure of the Madden-Julian Oscillation in the superparameterized CAM, *J. Atmos. Sci.*, *66*, 3277–3296, doi:10.1175/2009JAS3030.1.

Chatterjee, P., and B. N. Goswami (2004), Structure, genesis and scale selection of the tropical quasi-biweekly mode, *Q. J. R. Meteorol. Soc.*, *130*, 1171–1194, doi:10.1256/qj.03.133.

Collins, W. D., et al. (2006), The formulation and atmospheric simulation of the Community Atmosphere Model Version 3 (CAM3), *J. Clim.*, *19*, 2144–2161, doi:10.1175/JCLI3760.1.

DeMott, C. A., C. Stan, D. A. Randall, J. L. Kinter III, and M. Khairoutdinov (2011), The Asian monsoon in the super-parameterized CCSM and its relationship to tropical wave activity, *J. Clim.*, *24*, 5134–5156, doi:10.1175/2011JCLI4202.1.

Duchon, C. E. (1979), Lanczos filtering in one and two dimensions, *J. Appl. Meteorol.*, *18*, 1016–1022, doi:10.1175/1520-0450(1979)018<1016:LFIOAT>2.0.CO;2.

Goswami, B. N. (1998), Interannual variation of Indian summer monsoon in a GCM: External conditions versus internal feedbacks, *J. Clim.*, *11*, 501–522, doi:10.1175/1520-0442(1998)011<0501:IVOISM>2.0.CO;2.

Goswami, B. N. (2005), The Asian monsoon: Interdecadal variability, in *The Asian Monsoon*, chap. 7, edited by B. Wang, pp. 295–327, Springer, Berlin.

Goswami, B. N., and J. Shukla (1984), Quasi-periodic oscillations in a symmetric general circulation model, *J. Atmos. Sci.*, *41*, 20–37, doi:10.1175/1520-0469(1984)041<0020:QPOIAS>2.0.CO;2.

Goswami, B. N., and P. K. Xavier (2005), Dynamics of "internal" interannual variability of Indian summer monsoon in a GCM, *J. Geophys. Res.*, *110*, D24104, doi:10.1029/2005JD006042.

Goswami, B. N., G. Wu, and T. Yasunari (2006), Annual cycle, intraseasonal oscillations and roadblock to seasonal predictability of the Asian summer monsoon, *J. Clim.*, *19*, 5078–5099, doi:10.1175/JCLI3901.1.

Goswami, B. N., M. C. Wheeler, J. C. Gottschalck, and D. E. Waliser (2011), Intraseasonal variability and forecasting: A review of recent research, in *The Global Monsoon System: Research and Forecast, Ser. Asia-Pac. Weather and Clim.*, vol. 5, 2nd ed., edited by C.-P. Chang et al., pp. 389–408, World Sci., Hoboken, N. J.

Hendon, H. H., and M. C. Wheeler (2008), Some space-time spectral analyses of tropical convection and planetary-scale waves, *J. Atmos. Sci.*, *65*, 2936–2948, doi:10.1175/2008JAS2675.1.

Huffman, G. J., R. F. Adler, M. Morrissey, D. T. Bolvin, S. Curtis, R. Joyce, B. McGavock, and J. Susskind (2001), Global precipitation at one-degree daily resolution from multi-satellite observations, *J. Hydrometeorol.*, *2*, 36–50, doi:10.1175/1525-7541(2001)002<0036:GPAODD>2.0.CO;2.

Hurrell, J. W., J. J. Hack, D. Shea, J. M. Caron, and J. Rosinski (2008), A new sea surface temperature and sea ice boundary dataset for the Community Atmosphere Model, *J. Clim.*, *21*, 5145–5153, doi:10.1175/2008JCLI2292.1.

Jiang, X., T. Li, and B. Wang (2004), Structures and mechanisms of the northward propagation boreal summer intraseasonal oscillation, *J. Clim.*, *17*, 1022–1039, doi:10.1175/1520-0442(2004)017<1022:SAMOTN>2.0.CO;2.

Kalnay, E., et al. (1996), The NCEP/NCAR 40-year reanalysis project, *Bull. Am. Meteorol. Soc.*, *77*, 437–471, doi:10.1175/1520-0477(1996)077<0437:TNYRP>2.0.CO;2.

Khairoutdinov, M. F., and D. A. Randall (2001), A cloud resolving model as a cloud parameterization in the NCAR Community Climate System Model: Preliminary results, *Geophys. Res. Lett.*, *28*, 3617–3620, doi:10.1029/2001GL013552.

Khairoutdinov, M., and D. A. Randall (2003), Cloud-resolving modeling of ARM Summer 1997 IOP: Model formulation, results, uncertainties and sensitivities, *J. Atmos. Sci.*, *60*, 607–625, doi:10.1175/1520-0469(2003)060<0607:CRMOTA>2.0.CO;2.

Khairoutdinov, M., D. A. Randall, and C. DeMott (2005), Simulations of the atmospheric general circulation using a cloud-resolving model as a superparameterization of physical processes, *J. Atmos. Sci.*, *62*, 2136–2154, doi:10.1175/JAS3453.1.

Khairoutdinov, M., C. DeMott, and D. Randall (2008), Evaluation of the simulated interannual and subseasonal variability in an AMIP-style simulation using the CSU multiscale modeling framework, *J. Clim.*, *21*, 413–431, doi:10.1175/2007JCLI1630.1.

Kim, D., et al. (2009), Application of MJO simulation diagnostics to climate models, *J. Clim.*, *22*, 6413–6436, doi:10.1175/2009JCLI3063.1.

Krishna Kumar, K., K. Kamala, B. Rajagopalan, M. P. Hoerling, J. K. Eischeid, S. K. Patwardhan, G. Srinivasan, B. N. Goswami, and R. Nemanai (2011), Once and future pulse of Indian monsoonal climate, *Clim. Dyn.*, *36*, 2159–2170, doi:10.1007/s00382-010-0974-0.

Lin, J.-L., et al. (2006), Tropical intraseasonal variability in 14 IPCC AR4 climate models. Part I: Convective signals, *J. Clim.*, *19*, 2665–2690, doi:10.1175/JCLI3735.1.

Lin, J.-L., K. M. Weickman, G. N. Kiladis, B. E. Mapes, S. D. Schubert, M. J. Suarez, J. T. Bacmeister, and M.-I. Lee (2008), Subseasonal variability associated with Asian summer monsoon simulated by 14 IPCC AR4 coupled GCMs, *J. Clim.*, *21*, 4541–4567, doi:10.1175/2008JCLI1816.1.

Liu, P., et al. (2009), An MJO simulated by the NICAM at 14- and 7-km resolutions, *Mon. Weather Rev.*, *137*, 3254–3268, doi:10.1175/2009MWR2965.1.

Luo, Z., and G. L. Stephens (2006), An enhanced convection-wind-evaporation feedback in a superparameterization GCM (SP-GCM) depiction of the Asian summer monsoon, *Geophys. Res. Lett.*, *33*, L06707, doi:10.1029/2005GL025060.

Miura, H., M. Satoh, T. Nasuno, A. T. Noda, and K. Oouchi (2007), Madden-Julian Oscillation event realistically simulated by a global cloud-resolving model, *Science*, *318*, 1763–1765, doi:10.1126/science.1148443.

Oouchi, K., A. T. Noda, M. Satoh, B. Wang, S. P. Xie, H. G. Takahashi, and T. Yasunari (2009), Asian summer monsoon simulated by a global cloud-system-resolving model: Diurnal to intra-seasonal variability, *Geophys. Res. Lett.*, *36*, L11815, doi:10.1029/2009GL038271.

Pedlosky, J., and C. Frenzen (1980), Chaotic and periodic behavior of finite amplitude baroclinic waves, *J. Atmos. Sci.*, *37*, 1177–1196, doi:10.1175/1520-0469(1980)037<1177:CAPBOF>2.0.CO;2.

Rajeevan, M., J. Bhate, J. D. Kale, and B. Lal (2006), High-resolution daily gridded rainfall data for the Indian region: Analysis of break and active monsoon spells, *Curr. Sci.*, *91*, 296–306.

Sato, T., H. Miura, M. Satoh, Y. N. Takayabu, and Y. Wang (2009), Diurnal cycle of precipitation in the tropics simulated in a global cloud resolving model, *J. Clim.*, *22*, 4809–4826, doi:10.1175/2009JCLI2890.1.

Sikka, D., and S. Gadgil (1980), On the maximum cloud zone and the ITCZ over Indian longitudes during the southwest monsoon, *Mon. Weather Rev.*, *108*, 1840–1853, doi:10.1175/1520-0493(1980)108<1840:OTMCZA>2.0.CO;2.

Slingo, J. M., P. M. Inness, and K. R. Sperber (2005), Modeling, in *Intraseasonal Variability in the Atmosphere-Ocean Climate System*, chap. 11, pp. 361–397, edited by W. K.-M. Lau and D. E. Waliser, Springer, Heidelberg, Germany.

Sperber, K. R., J. M. Slingo, D. E. Waliser, and P. M. Inness (2008), Coarse-resolution models only partly cloudy, *Science*, *320*, 612a–613s, doi:10.1126/science.320.5876.612a.

Stan, C., M. Khairoutdinov, C. A. DeMott, V. Krishnamurthy, D. M. Straus, D. A. Randall, J. L. Kinter III, and J. Shukla (2010), An ocean-atmosphere climate simulation with an embedded cloud resolving model, *Geophys. Res. Lett.*, *37*, L01702, doi:10.1029/2009GL040822.

Tao, W.-K., et al. (2009), Multi-scale modeling system: Development, applications and critical issues, *Bull. Am. Meteorol. Soc.*, *90*, 515–534, doi:10.1175/2008BAMS2542.1.

Waliser, D. E. (2006), Intraseasonal variability, in *The Asian Monsoon*, edited by B. Wang, pp. 203–257, Springer, New York.

Waliser, D. E., et al. (2003), AGCM simulations of intraseasonal variability associated with the Asian summer monsoon, *Clim. Dyn.*, *21*, 423–446, doi:10.1007/s00382-003-0337-1.

Waliser, D., et al. (2009), MJO simulation diagnostics, *J. Clim.*, *22*, 3006–3030, doi:10.1175/2008JCLI2731.1.

Wang, B. (2005), Theory, in *Tropical Intraseasonal Oscillation in the Atmosphere And Ocean*, edited by W. K.-M. Lau and D. E. Waliser, chap. 10, pp. 307–351, Springer, Heidelberg, Germany.

Wang, B., and X. Xu (1997), Northern Hemisphere summer monsoon singularities and climatological intraseasonal oscillation, *J. Clim.*, *10*, 1071–1085, doi:10.1175/1520-0442(1997)010<1071:NHSMSA>2.0.CO;2.

Webster, P. J., V. O. Magana, T. N. Palmer, J. Shukla, R. A. Tomas, M. Yanai, and T. Yasunari (1998), Monsoons: Processes, predictability, and the prospects for prediction, *J. Geophys. Res.*, *103*, 14,451–14,510, doi:10.1029/97JC02719.

Wheeler, M., and G. N. Kiladis (1999), Convectively coupled equatorial waves: Analysis of clouds and temperature in the wave number-frequency domain, *J. Atmos. Sci.*, *56*, 374–399, doi:10.1175/1520-0469(1999) 056<0374:CCEWAO>2.0.CO;2.

Wilks, D. S. (1995), *Statistical Methods in the Atmospheric Sciences*, Academic, San Diego, Calif.

Yasunari, T. (1979), Cloudiness fluctuations associated with the Northern Hemisphere summer monsoon, *J. Meteorol. Soc. Jpn.*, *57*, 227–242.

J. J. Benedict and E. D. Maloney, Department of Atmospheric Science, Colorado State University, Fort Collins, CO 80523, USA.

B. B. Goswami, B. N. Goswami, N. J. Mani, and P. Mukhopadhyay, Indian Institute of Tropical Meteorology, Dr. Homi Bhabha Road, Pashan, Pune-411008, India. (mpartha@tropmet.res.in)

M. Khairoutdinov, School of Marine and Atmospheric Sciences, Stony Brook University, New York, NY 11794, USA.

D. E. Waliser, Jet Propulsion Laboratory, California Institute of Technology, Pasadena, CA 91109, USA.